Rapid #: -20069777

CROSS REF ID: **30336640210001852**

LENDER: **TET :: Charles C. Sherrod Library**

BORROWER: **ORU :: Main Library**

TYPE:	Article CC:CCG
JOURNAL TITLE:	Precambrian research
USER JOURNAL TITLE:	. Precambrian Research,
ARTICLE TITLE:	Why was there a Neoproterozoic Snowball Earth?
ARTICLE AUTHOR:	Retallack, G.J.,
VOLUME:	385,
ISSUE:	
MONTH:	
YEAR:	2023.
PAGES:	106952
ISSN:	0301-9268
OCLC #:	

Processed by RapidX: 1/9/2023 1:20:41 PM

Precambrian Research 385 (2023) 106952

Contents lists available at ScienceDirect

Precambrian Research

journal homepage: www.elsevier.com/locate/precamres

Why was there a Neoproterozoic Snowball Earth?

Gregory J. Retallack

Department of Earth Sciences, University of Oregon, Eugene, OR 97403-1272, USA

ARTICLE INFO

Keywords:
Cryogenian
Glaciation
Paleosols
Microfossils
Arizona

ABSTRACT

Snowball Earth is a nickname for the Cryogenian Period, 717 to 635 million years ago, when glaciers extended well into tropical latitudes. Such extreme planetary chilling has been blamed on increased carbon sequestration by life in the sea, by chemical weathering of volcanic rocks, and by life on land. Discovery of pre-Cryogenian paleosols containing a diverse eukaryotic soil microbiome including fungi and testate amoebae suggests that glacial expansion was caused by increased carbon consumption due to evolutionary advances in life on land. Microfossils in paleosols of the 776–729 Ma Chuar Group of Arizona include cyanobacterial microfossils (*Siphonophycus typicum* and *Polytrichoides linearis*), fungal hyphae (*Tortotubus protuberans* and *Mucorites ripheicus*), fungal vesicles (*Palaeoglomus strotheri*), and testate amoebae (*Cycliocyrillium torquatum, Trigonocyrillium horodyskii, Melanocyrillium hexadiadema, Bonneia dachrychares*, and *Carabinia granosa*). Also found were fragments of enigmatic lichen-like, multicellular thalli described here as *Porterra dehlerae* gen. et sp. nov. A few fossils by themselves did not change the world, but Chuar and other paleosols reveal transition from low productivity Gypsids to high productivity Calcids. Increased biomass, soil respiration, and nutrient depletion documented from chemical analyses of paleosols accelerated silicate weathering and carbon consumption, diminishing CO_2 greenhouse, and ushering in Snowball Earth.

1. Introduction

Neoproterozoic Snowball Earth (717–635 Ma) has been considered a time when the entire planet was covered by glaciers (Hoffman et al., 2017), but coeval loess and periglacial paleosols with sand wedges on unglaciated land have been found in paleotropical regions (Retallack, 2011b; Retallack et al., 2015; Liu et al., 2020). Although not totally ice covered, the Cryogenian Period was a time of unusually widespread glaciation (Hoffman et al., 2017). Four general explanations for this signal event in Earth history have been proposed: 1, evolutionary advances in life on land (Hedges, 2003; Kennedy, 2013); 2, evolutionary advances in marine life (Tziperman et al., 2011); 3, continental drift into warm-humid, tropical regions where weathering is more intense (Hoffman et al., 2017), or 4, large amounts of easily weatherable materials produced by unusually voluminous volcanism (Donnadieu et al., 2004; MacDonald and Wordsworth, 2017; Stern and Miller, 2018; Long et al., 2019; Arnscheidt and Rothman, 2020). The common thread to these ideas is diminished global greenhouse effect of atmospheric CO_2, either by reduction into biomass and soil organic matter (Tziperman et al., 2011), by neutralization of carbonic acid during silicate weathering (Donnadieu et al., 2004; MacDonald and Wordsworth, 2017; Hoffman et al., 2017; Stern and Miller, 2018; Long et al., 2019; Arnscheidt and Rothman, 2020), or by both (Hedges, 2003; Kennedy, 2013).

This study addresses theories for Snowball onset primarily from the perspective of newly discovered microfossils of the Chuar Group (776–729 Ma) of Grand Canyon National Park, Arizona (Retallack et al., 2021), here illustrated in further detail with description of a problematic new multicellular fossil, *Porterra dehlerae* gen. et sp. nov.. A few new microfossils do not explain the increase in silicate weathering intensity needed to induce global glaciation (Hedges, 2003; Tziperman et al., 2011; Hoffman et al., 2017; Arnscheidt and Rothman, 2020), so this paper also reviews increases in carbon sequestration and consumption from previously published Tonian paleosols in Arizona (Retallack et al., 2021) and Australia (Retallack, 2021). A global compilation of Cambrian to Tonian paleosols studied in detail chemically and petrographically can be used to calculate carbon sequestration by weathering (from base loss) and by biomass (from P loss: Table 1). These chemical data are supported by a large compilation of data of depths to calcic and gypsic horizons of paleosols as indications of CO_2 produced by soil respiration (Supplementary information Table S1).

2. Geological setting

The Chuar Group in the Grand Canyon is largely a shallow marine

E-mail address: gregr@uoregon.edu.

https://doi.org/10.1016/j.precamres.2022.106952
Received 31 March 2022; Received in revised form 9 December 2022; Accepted 20 December 2022
Available online 4 January 2023

sequence with stromatolitic and other dolostones and shales (Dehler et al., 2005), but also includes 66 paleosol horizons of 9 distinct pedotypes (Retallack et al., 2021). The paleosols are colored red and purple from hematite and organic matter mixtures. Paleosols are also recognized from distinctive cracking patterns, replacive calcite nodules, gypsum desert roses, geochemical negative strain and mass transfer, and highly correlated carbonate oxygen and carbon isotopic values (Retallack, et al., 2021). This study examines only one of those paleosols, the Sekawa silty clay loam, at 640 m stratigraphic level in the Carbon Canyon Member of the Galeros Formation, 400 m east of the campsite on Nankoweap Creek at the end of the Nankoweap Trail (Figs. 1A, 2A). The Sekawa paleosol has mottles of low-magnesium calcite forming a Bk horizon, similar to a modern Calcid soil (Retallack et al., 2021). Unlike other red and oxidized paleosols in the same local section, the Sekawa profile has elevated molar ratios of soda/potash as evidence of salinization, high alkaline earth/alumina ratios of calcification, and elevated ferrous/ferric ratios of modest gleization (Fig. 2B). This distinctive pickling and chemical reduction may explain why it, and not other red or purple paleosols of the Chuar Group have recently yielded a variety of microfossils permineralized by silica cement (Retallack et al., 2021). Microfossil organic walls are poorly preserved and ferruginized, but their central cavity is filled with silica (Figs. 3-5). These microfossils were liberated from the matrix by dissolving clayey matrix in hydrofluoric acid that destroyed minerals other than quartz, and reveal a diverse terrestrial microbiome dated at 758 Ma from an age model based on interpolation of local radiometric dates (Retallack et al., 2021).

3. Materials and methods

Detailed measured sections for sampling were made of red beds in the Carbon Canyon Member of the Galeros Formation along Nankoweap Creek, 1.1 km upstream of the narrow gorge to the Colorado River at

Table 1
Estimates of global carbon sequestration from Stenian to Cambrian paleosols.

Ma	location	Soil formation (years)	MAP (mm)	Depth water (cm)	Base loss (mol mm^{-1} a^{-1})	P loss (mol mm^{-1} a^{-1})	Land area (10^6 km)	Global C from base loss (g a^{-1})	error 2 × s.d.	Global C from P loss (g a^{-1})	error 2 × s.d.	References
503	Elk Point, Wisconsin	100,000	1502	422	1.02	0.04	951.20	1.97E + 14	52.07	8.37E + 12	2658.15	1
504.9	Wirrealpa, S. Austral.	6600	426	80	0.43	0.04	950.91	8.35E + 13	22.04	8.64E + 12	1124.93	2
508.6	Wirrealpa, S. Austral.	500	551	76	0.27	0.02	950.367	5.14E + 13	13.57	3.78E + 12	692.00	2
508.6	Wirrealpa, S. Austral.	8800	599	224	0.33	0.03	950.37	6.28E + 13	16.59	5.60E + 12	846.16	2
508.6	Wirrealpa, S. Austral.	1000	324	46	0.11	0.01	950.37	2.16E + 13	5.70	2.87 + 12	290.66	2
508.6	Wirrealpa, S. Austral.	6600	426	119	0.95	0.05	950.37	1.83E + 14	48.23	9.99E + 12	2460.22	2
523.5	Wirrealpa, S. Austral.	2000	426	86	1.31	0.03	948.16	2.53E + 15	66.72	6.45E + 12	3395.16	2
539.8	Parachilna Gorge, S.A.	500	909	98	0.04	0.12	945.75	7.13E + 12	1.88	2.32E + 13	95.49	2
539.9	Parachilna Gorge, S.A.	7300	456	74	0.05	0.04	945.73	9.03E + 12	2.38	7.38E + 12	120.97	2
549.3	Brachina Gorge, S.A.	100	200	63	2.64	0.52	944.34	5.07E + 14	133.64	1.00E + 12	6773.74	3
549.5	Brachina Gorge, S.A.	1000	344	85	0.12	0.05	944.31	2.23E + 13	5.88	9.84E + 12	298.26	3
549.5	Brachina Gorge, S.A.	1000	204	69	0.50	0.14	944.31	9.53E + 13	25.16	2.66E + 13	1275.02	3
549.5	Brachina Gorge, S.A.	1000	344	136	0.08	0.49	944.31	1.48E + 13	3.91	9.42E + 13	198.20	3
557.3	Brachina Gorge, S.A.	5000	400	63	0.01	0.02	943.16	1.31E + 12	0.34	3.53E + 12	17.45	3
558	Pada Aru, Estonia	500,000	1000	5719	0.03	0.00	943.06	5.39E + 12	1.42	6.00E + 11	71.92	4
558	Lohu, Estonia	500,000	1000	3012	0.05	0.05	943.06	1.05E + 13	2.78	8.90E + 12	140.87	4
635	Enorama Creek, S.A.	6000	400	199	0.20	0.01	931.66	3.88E + 13	10.24	2.71E + 12	511.84	5
706	Ellery Creek, N.Territory	5900	291	63	0.17	0.04	921.15	3.11E + 13	8.20	7.63E + 12	405.44	6
720	Ellery Creek, N.Territory	47,400	142	68	0.02	0.01	919.08	3.77E + 12	1.00	1.05E + 13	49.12	6
758	Nankoweap Ck, Arizona	1000	284	45	3.41	0.17	913.46	6.33E + 14	167.01	3.14E + 13	8188.25	6
759	Nankoweap Ck, Arizona	8800	386	58	0.01	0.01	913.31	1.36E + 12	0.36	1.29E + 12	17.61	6
770	Nankoweap Ck, Arizona	11,800	132	131	0.08	0.06	911.68	1.49E + 13	3.94	1.20E + 13	192.66	6
810	Sheigra, Scotland	100,000	1000	717	0.01	0.01	905.76	2.09E + 12	0.55	2.13E + 12	26.78	7
810	Sheigra, Scotland	100,000	683	489	0.43	0.04	905.76	7.87E + 13	20.77	8.10E + 12	1009.57	7
1100	Sturgeon Falls, Michigan	13,000	1000	851	0.57	0.00	862.84	1.00E + 14	26.44	7.59E + 11	1224.30	8

Note: References are (1) Horodiskyj (2012); (2) Retallack (2008), (3) Retallack (2013b), (4) Liivamägi et al., (2015), (5) Retallack (2011b), (6) Retallack (2021), (7) Retallack et al. (2021), (7) Retallack and Mindszenty (1994), (8) Zbinden et al. (1988).

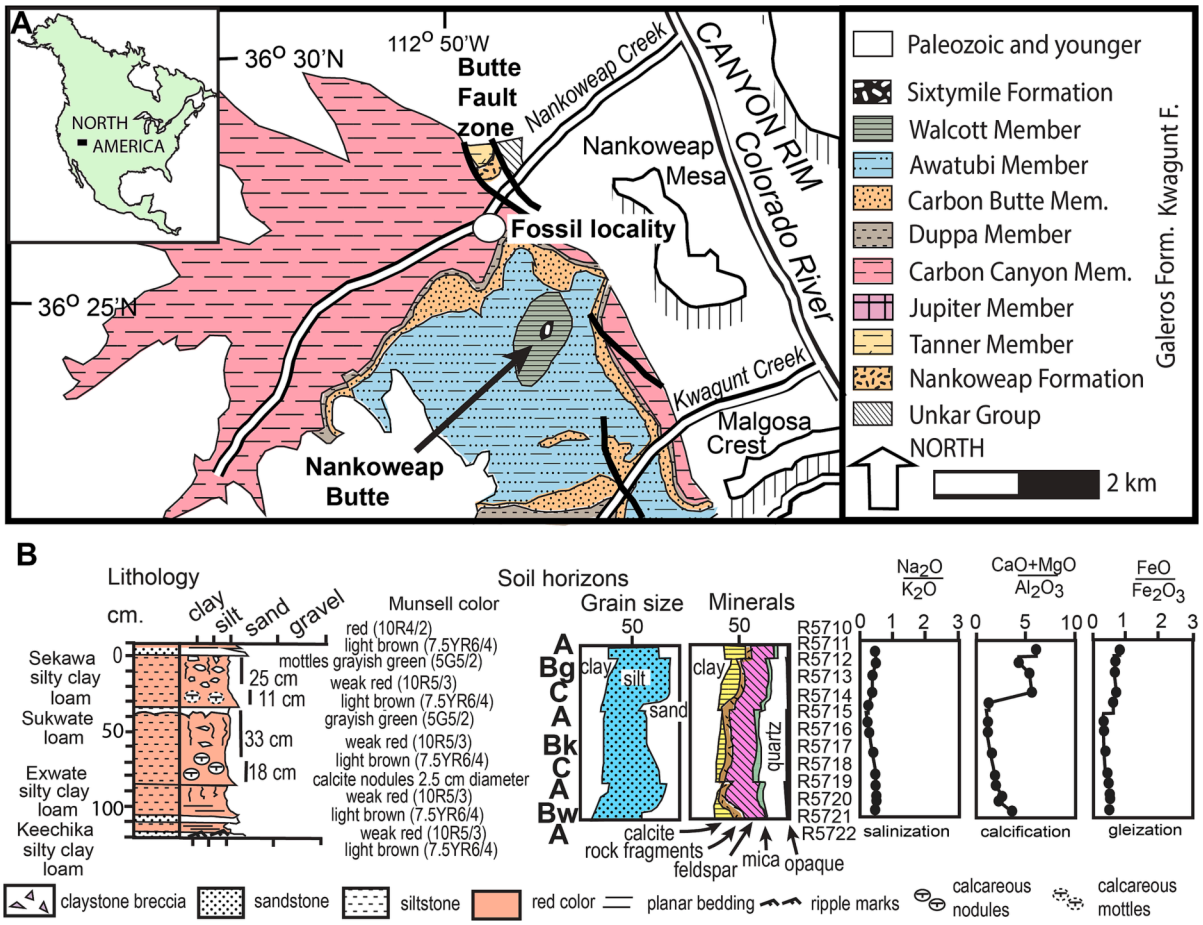

Fig. 1. Geological map (A) and section (B) of fossiliferous paleosols in the Tonian (792 Ma), Carbon Canyon Member of the Chuar Group, Grand Canyon, Arizona (Dehler et al., 2005). This area has only small outcrops of Sixtymile Formation atop Nankoweap Butte and Jupiter Member in splays of Butte Fault.

N36.279293° W111.89076° (Fig. 1A). Oriented rock samples were collected and archived in the Museum of Natural and Cultural History of the University of Oregon. Thin sections were used to quantify grain size and mineral compositions (Fig. 1B) by point counting (500 points) using a Swift automated stage and Hacker counting box on a Leitz Orthoplan Pol research microscope. Major and trace element chemical analysis was determined by XRF from fused beads at ALS Chemex in Vancouver, Canada (Retallack et al., 2021). Silica-filled microfossils were macerated from the red beds using 48 % HF, and neutralizing with NaOH, then mounted on metal stubs for examination in the QANTA ESEM-VPSEM Scanning Electron Microscope in the CAMCOR analytical laboratories of the University of Oregon. Also included is a compilation of depth to calcic and gypsic horizons of 7342 previously published paleosols (see Supplementary Information Online Table S1).

4. Paleosol microbiome discovered

A surprising discovery made during study of the Sekawa paleosol of the Chuar Group (Retallack et al., 2021) was a variety of microfossils, which were not contaminants from the modern outcrop for the following reasons. The fresh rock outcrop was quarried back to obtain large fist-sized samples suitable for making petrographic thin sections, which first revealed the microfossils (Fig. 2B-F) completely enclosed without access tubes from the surface. Fossils from the same fresh rock samples were then dissolved in hydrofluoric acid, with the result that the acid-resistant, lithified, fossils revealed were identical with others already recorded from silicified rocks of the Chuar Group, rather than the most similar modern material illustrated by Porter et al. (2003). The partly silicified fossils were also compacted by burial alteration to at least 57 % of original inflated diameter, as predicted from known overburden and thermal maturity of organic matter (Retallack et al., 2021), and organic fossils were completely flattened (Fig. 3G-I). Because some of these fossils have long been considered marine (Schopf et al., 1973; Porter et al., 2003), could they have been a part of the marine parent material to the Sewaka paleosol or blown in from the sea during the Precambrian? Both sources of contamination are falsified by the distribution of the fossils which are locally abundant but scattered within the soil rather than deposited in layers (Fig. 2B). Furthermore, the sedimentary parent material of this 30-m-thick sequence of paleosols above a 20-m-thick fluvial paleochannel does not include stromatolites, lamination, or other indications of marine conditions (Retallack et al., 2021).

The taphonomy of the microfossils is similar to those previously described from the Chuar Group, including both silicified (Schopf et al., 1973; Porter et al., 2003) and organically preserved remains (Agić and Cohen, 2021; Woltz et al., 2021), preserved by burial reduction of organic matter and early diagenetic silicification. Some of the silicified cavities of the fossils lacked organic coating (Fig. 3B, 4A-B,G), or had only partial organic collars (Fig. 4E-F). Completely organic fossils unsupported by silica cement were deformed by flattening, but retained ornament (Fig. 3G-I).

Although Precambrian paleosols have been modelled as abiotic (Rye and Holland, 1998), biological features of the Sekawa paleosols include drab-haloed filament traces and cracks visible in the field (Fig. 2A) and in thin section (Fig. 2B). These common features of red paleosols are called *Prasinema gracilis* and attributed to burial gleization of rope-forming cyanobacteria or other filamentous microbes (Retallack, 2011a). Comparable features of rope-forming cyanobacteria were also seen in macerated permineralized specimens under scanning electron

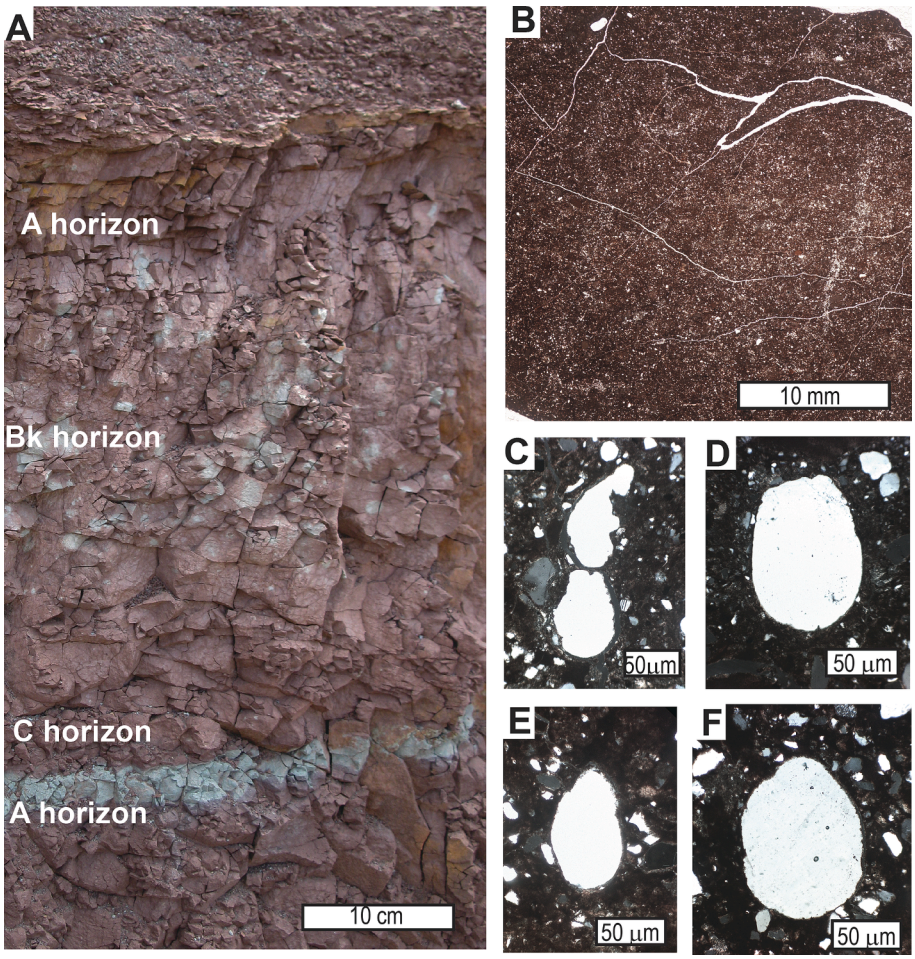

Fig. 2. Tonian (758 Ma), Sekawa silty clay loam paleosol in outcrop, showing paleosol horizon designations of Fig. 1B (A), in thin section scan (B), and details of testate amoebae, *Cycliocyrillium torquatum* (C-F); C, asexual cell division, well known in testate amoebae (Porter et al., 2003); B-F, Museum of Natural and Cultural History, University of Oregon specimen F127365 = R5711.

microscope, showing fine filaments with adhering matrix (Fig. 3A). These new observations add to petrographic observations of internal structure and of context (Retallack, 2011a, 2012), to counter the opinion of Jago et al. (2012) that *Prasinema* may be a pseudofossil.

Another common microfossil is a smooth sheath, surrounding subparallel fine filaments (Fig. 3C), comparable with *Polytrichoides linearis*, considered a rope-forming cyanobacterium (Li et al., 2019). *Siphonophycus typicum* (Fig. 3B) may also be a polysaccharide sheath of a cyanobacterium (Li et al., 2019). Other tubular features have an echinate sheath and attached lateral vesicles (Fig. 3D), comparable with the fungal fossil *Tortotubus protuberans* (Smith, 2016). *Tortotubus* has been considered a dikaryan fungus (Smith, 2016), but lacks clear dikaryan features such as clamp connections, so could equally be a glomeromycotan or mucoromycotinan cord (Retallack et al., 2013; Loron et al., 2019). Glomeromycota include mycorrhizal fungi (Retallack, 2019). Proterozoic fossil vesicles (Retallack, 2015a) and spores (Loron et al., 2019) demonstrate that such fungi predate the evolution of plants (Retallack, 2019; Strother and Foster, 2021). Hyphae with ellipsoidal bodies at septal partitions (Fig. 3E-F) appear to be mucoromycotinan fungi, *Mucorites ripheicus* (Hermann and Podkovyrov, 2006). Although Taylor et al. (2015) doubt the affinities of *M. ripheicus* preserved as flattened macerals, the new material confirms their morphology in three dimensions with chipping and cracking as evidence of silicification (Fig. 3E-F), so not modern contamination. Another fungal fossil in the Sekawa paleosol is rugulate vesicles (Fig. 3G-I), comparable with the fossil glomeromycotan *Palaeoglomus strotheri* (Retallack, 2019).

The most conspicuous fossils in paleosol thin sections are testate amoebae filled with secondary quartz (Schopf et al., 1973; Porter et al., 2003). In thin section, they look like consistently shaped, obovate to ellipsoidal quartz grains (Fig. 2C-F), but when isolated from matrix they have a distinctive shagreen ("coat of mail") texture (Fig. 4A-B,G), from impressions of small organic scales. Others have preserved organic remnants of the terminal orifice showing both inner and outer wall with recessive space between (Fig. 4E-G), and included scales on the body (Fig. 4F, H). These organic remains are poorly preserved in the Sekawa paleosol, as expected from its highly oxidized condition (Retallack, et al., 2021), so that these testate amoebae are not as well preserved as those within black shales and carbonates of the Chuar Group (Porter et al., 2003). Some of these fossils appear to be reproducing asexually from the aperture (Fig. 2C), as noted in both modern and fossil testate amoebae (Porter et al., 2003). Some wall fragments have lunate holes (Fig. 4I), like those interpreted as predation holes from vampyrellid amoebae (Porter, 2016). Macerated specimens are preserved as internal molds of quartz (Fig. 4A-C), as incompletely crystal-filled tests with wall and aperture remnants (Fig. 4E-G), or as agglutinated tests (Fig. 4H). These vase-shaped microfossils are identified with Chuar Group fossil species described by Porter et al. (2003): *Cycliocyrillium torquatum* (Fig. 4A-B), *Trigonocyrillium horodyskii* (Fig. 4C-D), *Melanocyrillium hexadiadema* (Fig. 4E), *Bonniea dacruchares* (Fig. 4F-G), and *Carabinia granosa* (Fig. 4H). Hundreds of potential specimens were seen in thin section (Fig. 2B), but of 38 identifiable specimens scanned on SEM stubs, there were 12, 8, 7, 6, and 5 clear examples each of the five species listed in order. Each species was morphologically consistent in overall shape and size.

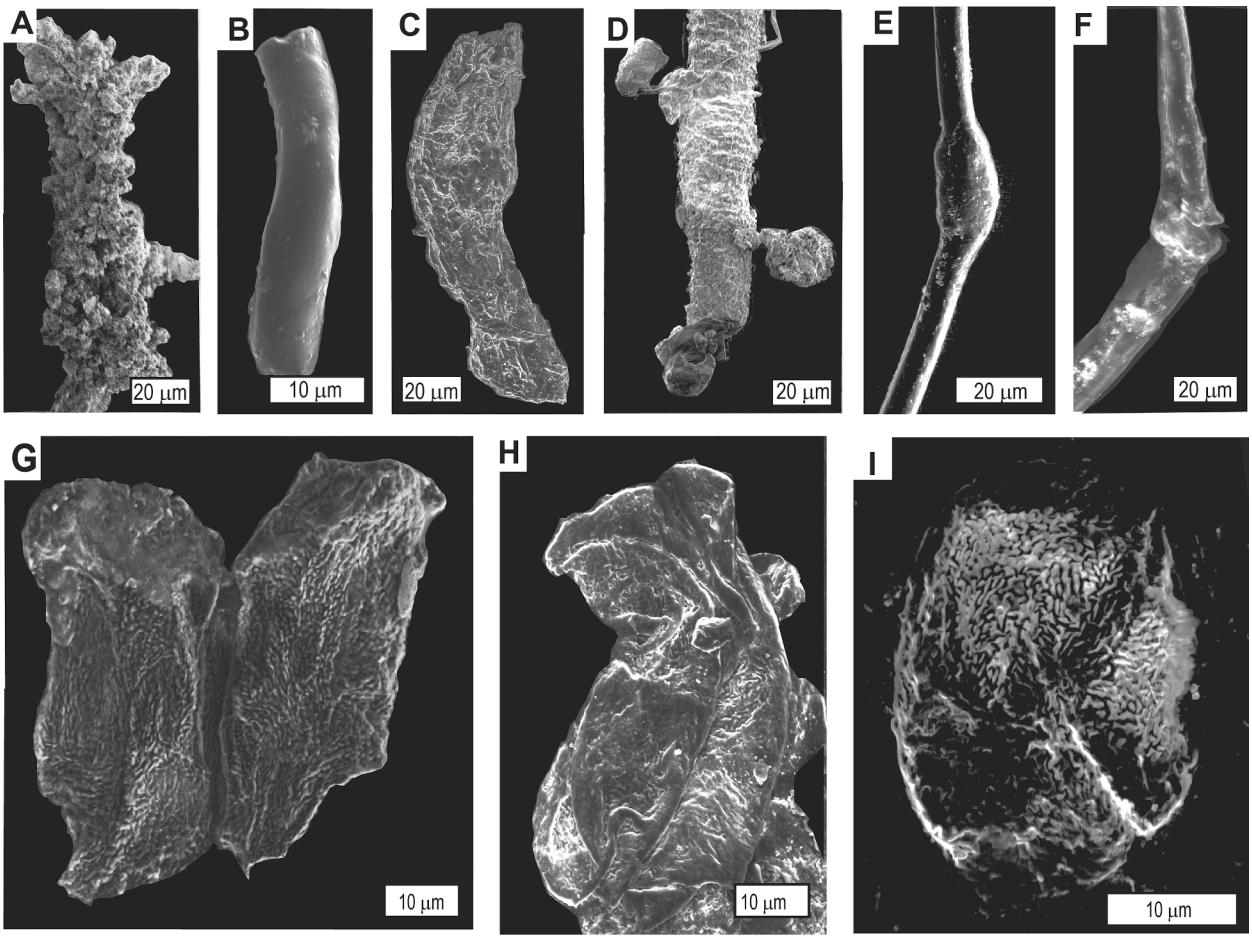

Fig. 3. Cyanobacteria (A-C) and fungi (D-F), permineralized by silica in the Tonian (758 Ma), Sekawa paleosol: A, *Prasinema gracile* (Retallack, 2011a), stub F127276; b, *Siphonophycus typicum* (Li et al., 2019), F127278; c, *Polytrichoides linearis* (Li et al., 2019), both on stub F127278; d, *Tortotubus protuberans* (Smith, 2016), F127283; e, *Mucorites* ripheicus (Hermann and Podkovryov, 2006), F127363; G-I, *Palaeoglomus* sp. cf. *P. strotheri* (Retallack, 2019), F127363.

Multicellular thallus fragments are also present (Fig. 5). They were at first considered pumice clasts, but lack massive glass between bubbles, showing instead a seam where adjacent, polygonal, organic, cell walls were adpressed by deformation associated with burial compaction (Fig. 5F). Acid treatment would have dissolved pumice more than silica fill, so that divisions would be grooves, rather than protruding double walls. These multicellular fragments are unsilicified organic remains like those of vesicles (Fig. 3G-I) and amoebal pellicles (Fig. 4E-F) from the same rock. These enigmatic multicellular remains are here called *Porterra dehlerae* gen et sp. nov., and are unlike other Precambrian cell aggregates (Strother and Wellman, 2016; Li et al., 2019; Agić et al., 2019) in having interlocking large pseudoparenchyma (40 μm) penetrated and surrounded by narrow (6 μm) haustoria and hyphae. The haustoria are unlike those of lichens in which the algal symbiont is small, rounded, and encircled (Retallack, 2019), rather than large, polygonal, and embayed (Fig. 5E-F). These fragments may be fungally infected green or red algae, perhaps even mycoheterotrophs, which are parasitic on fungi (Gomes et al., 2019). There is no sign of haustorial branching or arbuscles as found in modern and fossil mycorrhizae (Retallack, 2019). They could also be aggregated fungal vesicles (Retallack, 2015a, 2019; Loron et al., 2019). There is no indication of necrosis and fragmentation of walls expected in dead thalli of algae or colonial cyanobacteria decayed by fungi. These multicellular fragments are up to 0.5 mm long, but have some finished edges, like radiating cells of a lobate thallus. Mesoproterozoic multicellular cell aggregates are widely known (Li et al., 2019), but *Porterra* shows a degree of organization and adhesion suggestive of megascopic life. Regardless of biological affinities, evidence for multicellular life on land demonstrates a path toward increased biomass, carbon sequestration, and weathering on land, as also envisaged for geologically later evolution of non-vascular land plants (Lenton et al., 2012).

Comparable microfossils, including cyanobacteria, fungi, and testate amoebae have been known from the Chuar Group for many years, but were assumed to have been marine because found in nodular and pisolitic black shales (Porter et al., 2003; Dehler et al., 2005). That facies may indeed be marine (Fig. 6E), but not necessarily where the microfossil organisms lived (Retallack et al., 2021). Testate amoebae today are predators of bacteria and fungi in soils (Mitchell et al., 2008). The microfossils described here are geologically older than previously described testate amoebae considered marine (Porter et al., 2003), and are evidence for a terrestrial origin of testate amoebae.

5. Systematic paleontology

5.1. Kingdom fungi?

5.1.1. Family and division incertae sedis

5.1.1.1. Genus. Porterra gen. nov. (Fig. 5). New generic name registered with Mycobank (https://www.mycobank.org/) as 843,541.

5.1.1.2. Etymology. The generic name is in honor of Susannah M. Porter, in elision with Latin *terra* (f.), earth.

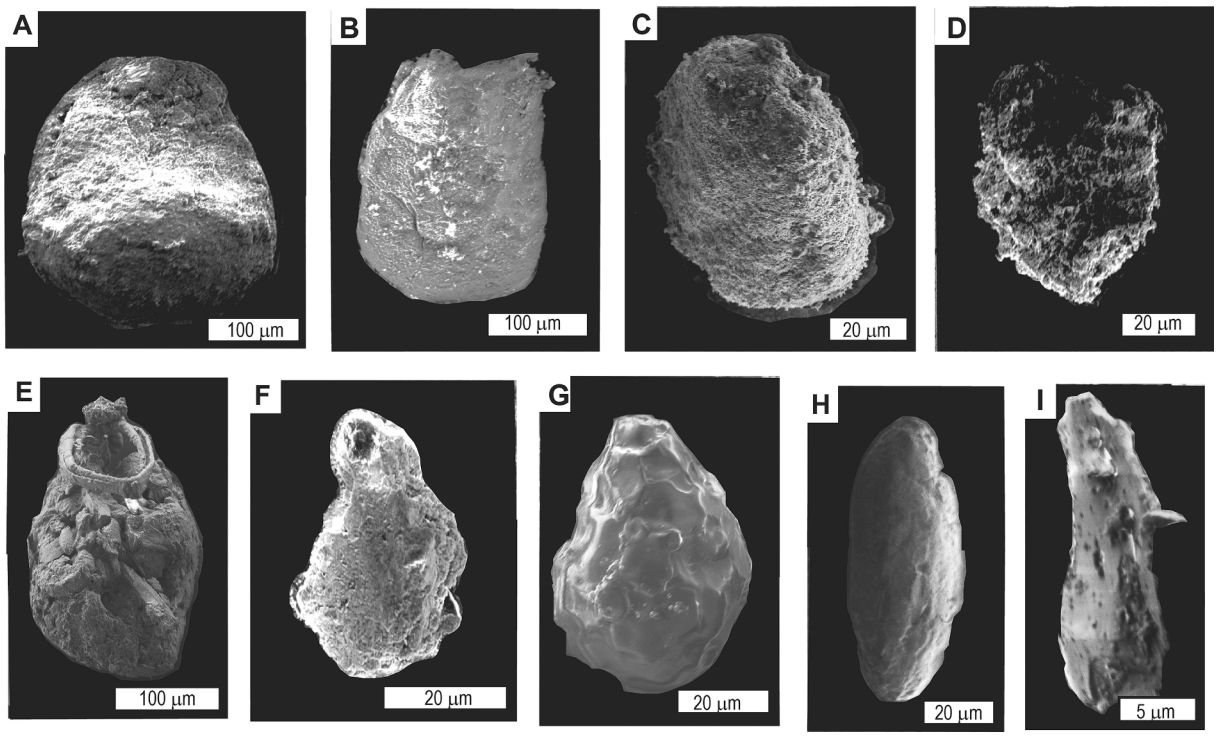

Fig. 4. Amoebozoans permineralized by silica in the Tonian (758 Ma) Sekawa paleosol: A-B, *Cycliocyrillium torquatum*, F127277 and F127279; C-D, *Trigonocyrillium horodyskii*, F; E, *Melanocyrillium hexadiadema*, F127362; F-G, *Bonneia dacruchares*, F127278; H, *Carabinia granosa*, F127276; I, wall fragment with predation holes, FR5713.

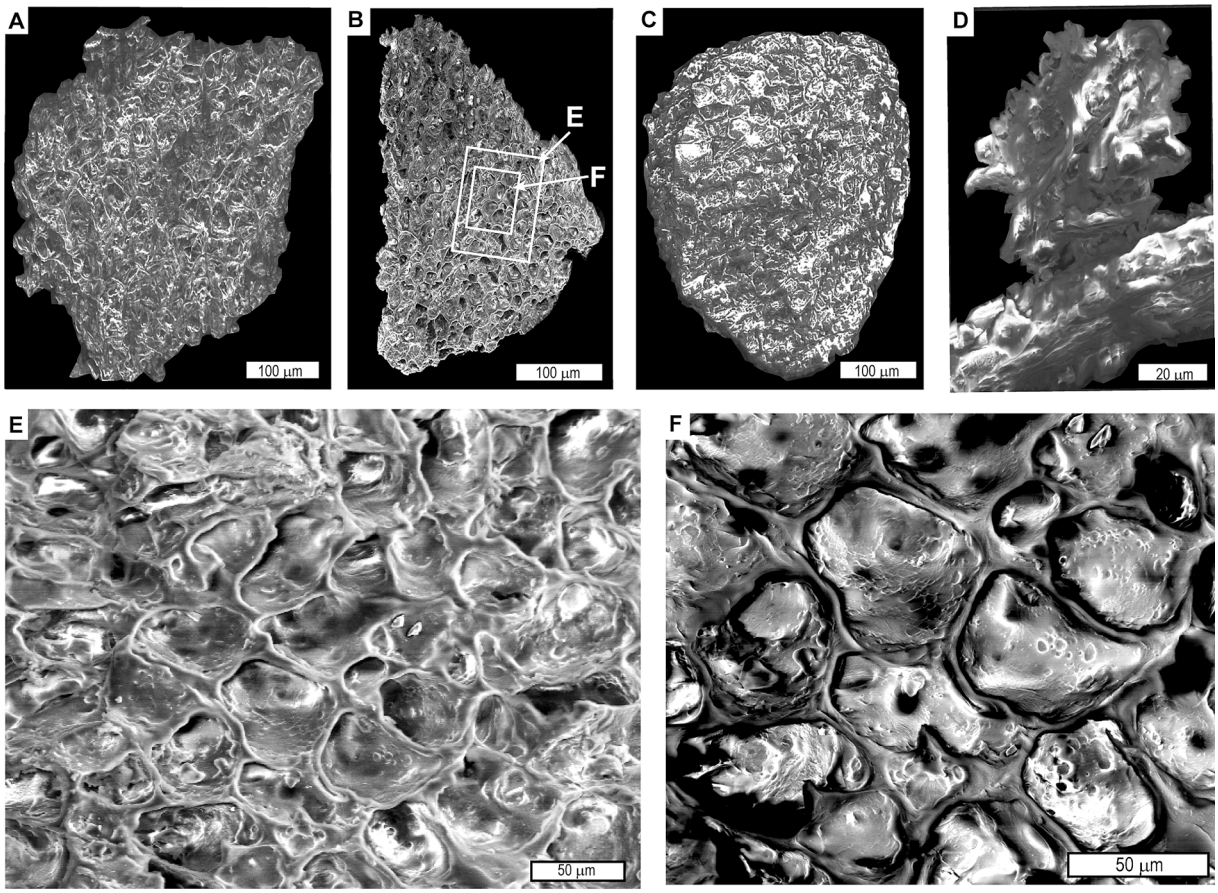

Fig. 5. *Porterra dehlerae* gen. et sp. nov., A-C thallus fragments; D,?rhizine; E-F detail of adpressed cells with hyphal intrusion at positions indicated in panel B which is the holotype; all F127282.

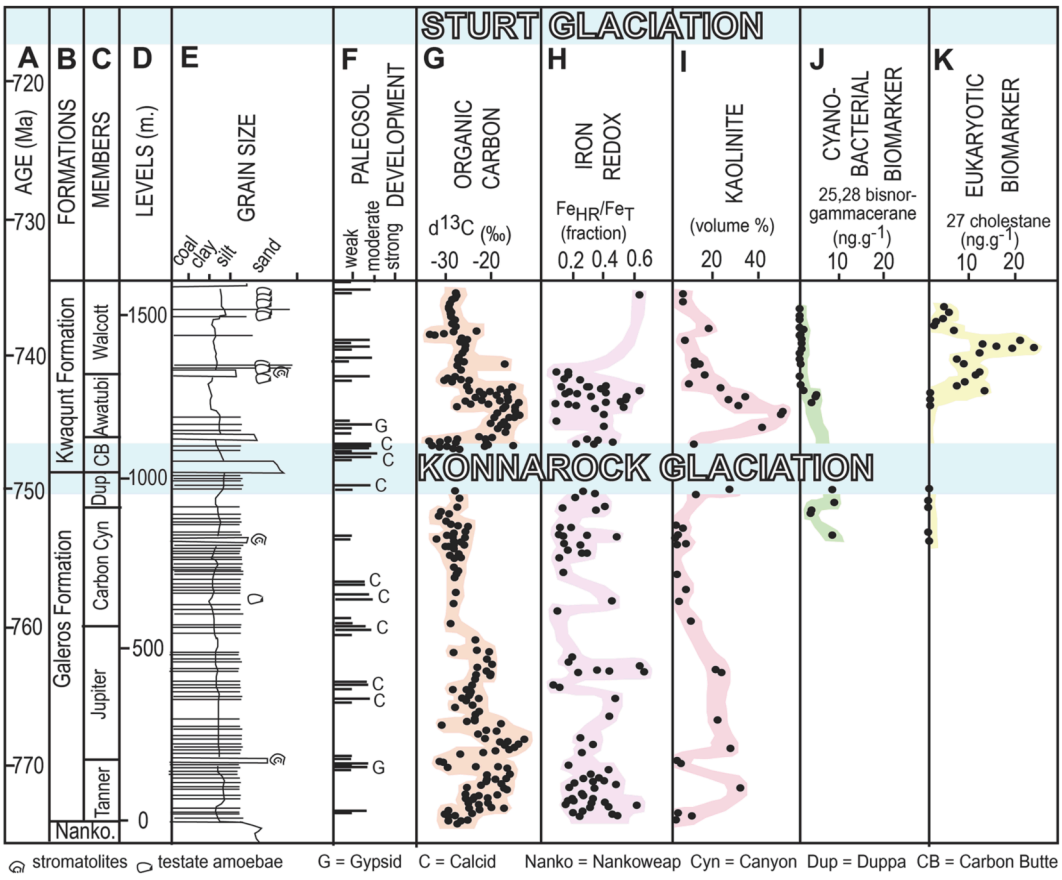

Fig. 6. Geological section and age model of the Chuar Group (A-C) with positions and degree of development of paleosols (D) and a variety of paleoenvironmental proxies (G-K); A-F, section, age model and paleosols (Retallack et al., 2021); G, carbon isotopic composition of organic matter (Dehler et al., 2005); H, highly reactive to total iron (Johnston et al., 2010); I, kaolinite (Dehler et al., 2005); J, cyanobacterial biomarker 25,28 bisnorgammacerane (van Maldegem et al., 2019); K, eukaryotic fungus, red alga or animal biomarker 27 cholestane (van Maldegem et al., 2019). (For interpretation of the references to colour in this figure legend, the reader is referred to the web version of this article.)

5.1.1.3. Type species. Porterra dehlerae sp. nov. New specific epithet registered with Mycobank (https://www.mycobank.org/) as 843,542.

5.1.1.4. Generic diagnosis. Multicellular thallus fragments of irregularly shaped and sized, polygonal pseudoparenchyma cells, 40–60 μm in diameter, with closely adpressed walls: cell walls indented and linked by hollow short haustoria and elongate hyphae; pseudoparenchyma cells forming radiating arrays of a lobate thallus.

5.1.1.5. Remarks. Porterra dehlerae is most like the enigmatic *Cyathinema digermulense* (Agić et al., 2019), an Ediacaran multicellular thallus with large and small cells that are narrower (<7 μm) and tubular, unlike *Porterra*. Sheets of Ordovician tetrad spores *Grododowon orthogonalis* (Strother et al., 2017), may have been terrestrial charophytes also represented by cryptospores (Strother and Foster, 2021). *Grododowon* is more regularly ranked and lacks associated hyphae of *Porterra*. Other Mesoproterozoic multicellular aggregates from palynological preparations (Strother and Wellman, 2016; Li et al., 2019) include loosely aggregated spherical to ovoid vesicles in subspherical clusters (*Synsphaeridium*, *Squamosphaera*, *Eohalothece*), sheets (*Ostiana*, *Myxococcoides*) and tubes (*Chlorogloeaopsis*, *Polysphaeroides*), but all have subspherical cells not so closely adpressed or accommodating each other, and without linking haustoria of *Porterra*. Large cells with hyphae attached are also similar to the vesicles of Paleoproterozoic *Diskagma*, and similar living *Geosiphon*, which contains symbiotic nostocalean cyanobacteria (Retallack et al., 2013). The biological affinities of *Porterra* are uncertain: possibilities include aggregated fungal vesicles, lichenized algae, alga with mycorrhiza, mycoheterotroph, or fungal decay of algae or colonial cyanobacteria.

5.1.1.6. Species. Porterra dehlerae sp. nov. (Fig. 5).

5.1.1.7. Etymology. The specific epithet is in honor of Carol M. Dehler.

5.1.1.8. Holotype. University of Oregon Museum of Natural and Cultural History SEM stub UOF127282 (Fig. 5B).

5.1.1.9. Specific diagnosis. Thallus fragments cuneate and dichotomizing, or ovate in shape, up to 0.5 mm long: parenchyma cells polygonal with closely adpressed walls, 45 ± 15 μm diameter (n = 109), linked and penetrated by haustoria and hyphae 6 ± 2 μm in diameter (n = 101).

6. Chemical weathering increase from paleosols

Documentation of terrestrial microbiomes is necessary, but insufficient evidence to address the role of soil carbon sequestration in global change toward Snowball Earth. A few fossils in paleosols does not constitute evidence of increased carbon sequestration on land, which requires independent evidence for changed weathering regimes (Fig. 6A-D) from paleosols (Fig. 6E), clay minerals (Fig. 6I), and biomarkers (Fig. 6J-K) of the Chuar Group. Recognition of paleosols in the Chuar Group (Fig. 6F) is confirmed by isotopically light carbon (Fig. 6G) and highly-reactive/total iron ratios (Fig. 6H), that are very low (<0.2),

as in soils (Ku et al., 2008; Johnston et al., 2010). Low isotopic values of carbon correspond to marine regression and exposure both during the 717 Ma Sturt Glaciation (Hoffman et al., 2017), and the 751 Ma Konnarock Glaciation (MacLennan et al., 2020). Spikes in kaolinite abundance reveal episodes of intense terrestrial weathering (Dehler et al., 2005). Declining abundance of cyanobacteria is reflected in decreasing abundance of the biomarker 25,28 bisnorgammacerane through the Chuar Group, and increased abundance of eukaryotes, including testate amoebae, red algae, or fungi are revealed by increasing C27-cholestane (van Maldegem et al., 2019). This particular sterane has been interpreted as diagnostic for animals (Bobrovskiy et al., 2018), but is also widespread in red algae and fungi (Retallack, 2020).

Comparable increases in paleosol productivity from 785 to 717 Ma have also been documented from the Johnnies Creek Formation of the Bitter Springs Group in Central Australia. Increased depth to salts was observed in Gypsid then Calcid paleosols of the Bitter Springs Group, and also plausible megafossils (Retallack, 2021). The Gypsid to Calcid change in weathering documented in paleosols of both the Chuar (Retallack et al., 2021) and Bitter Springs Groups (Retallack, 2021), can be compared with the transition in the modern Atacama Desert from gypsic cyanobacterial-actinobacterial microbiomes to calcic fungal-algal microbiomes sequestering 6 times more soil organic carbon (Ewing et al., 2008). Lichens are largely responsible for the difference today, as laboratory studies have shown that weathering intensity under modern lichens is 2–71 times that of nearby abiotic rock surfaces (Brady et al., 1999; Schwartzmann, 2017).

Another line of evidence for increased Neoproterozoic weathering is increased depth of gypsic and calcic horizons in paleosols, which is a proxy for late growing season soil respiration. The relationship between depth to salts and late growing season soil respiration, as a proxy for productivity, is based on modern soils in which soil CO_2 has been monitored (Breecker and Retallack, 2014). Key field measurements compiled for this study was depth to the salt horizon (Bk or By: see Supplementary Information online). The depth measured in paleosols in the field can be compared with modern soils after correction for burial compaction (C, fraction) calculated from depth of burial (B, km) by equation 1 in which 0.51, 0.49, and 0.27, are solidity, initial porosity and a fitting constant, respectively, for Aridisol soils (Sheldon and Retallack, 2001). These calculations are locality specific and from references to the paleosols in Supplementary Information online.

$$C = \frac{-0.51 \times 100}{\left\{\left(\frac{0.49}{\frac{B}{e^{0.27}}}\right) - 1\right\}} \quad (1)$$

Respired soil CO_2, as a proxy for secondary productivity, increases with mean annual precipitation and depth to salts in soils. Seasonal variation in soil CO_2 is large, ranging from a peak during spring regrowth and a low in winter dormancy, but late growing season soil CO_2 is critical to precipitation of calcite and gypsum in soils (Breecker and Retallack, 2014). Depth to gypsic (D_g, cm) and calcic (D_c, cm) horizons in soils are related to late growing season soil CO_2 (C_r, ppm), by equations 4 ($r^2 = 0.66$, s.e.=±768, $p = 0.0001$) and 5 ($r^2 = 0.64$, s.e.=±552, $p = 0.05$).

$$C_r = 25.3D_c + 588 \quad (2)$$

$$C_r = 42.9D_g + 399 \quad (3)$$

Soil erosion compromises these relationships, which are not applicable to soils of hillslopes and erosional landscapes (Royer, 1999). Equations 2 and 3 were based only on Holocene soils of sedimentary parent materials in aggrading fluvial floodplains, and applied to long sequences of alluvial sedimentary rocks (Retallack, 2005; Retallack and Huang, 2010). Some paleosols were flagged for erosion by overlying paleochannels or lack of converging root traces toward the surface (Retallack, 1983; Retallack et al., 2000). Depths to salts in long stratigraphic sequences show striking consistence and cycles of paleoclimate in stratigraphic successions (Retallack et al., 2004; Retallack, 2009a,b). Most important for onset of the Croyegnian ice age is increased depth of salts and corresponding incease in soil respiration in the late Tonian (Figs. 7A-B, 8).

7. Global carbon sequestration model

Calculating global carbon consumption by biomass and silicate weathering has proven possible with Pleistocene and middle Miocene paleosols (Retallack, 2022a). Fundamental to this effort is a sophisticated method to disentangle soil formation from sedimentation by tau analysis (Brimhall et al., 1992), which isolates two separate aspects of weathering: mole fraction mass transport ($\tau_{j,w}$) of a mobile element and mole fraction strain ($\varepsilon_{i,w}$) of an immobile element, using the following equations 3 and 4, including bulk density (ρ in g.cm^{-3}) and oxide assay (C in weight %) for successive samples (subscripts i,j) of weathered material (subscript w) and parent material (subscript p).

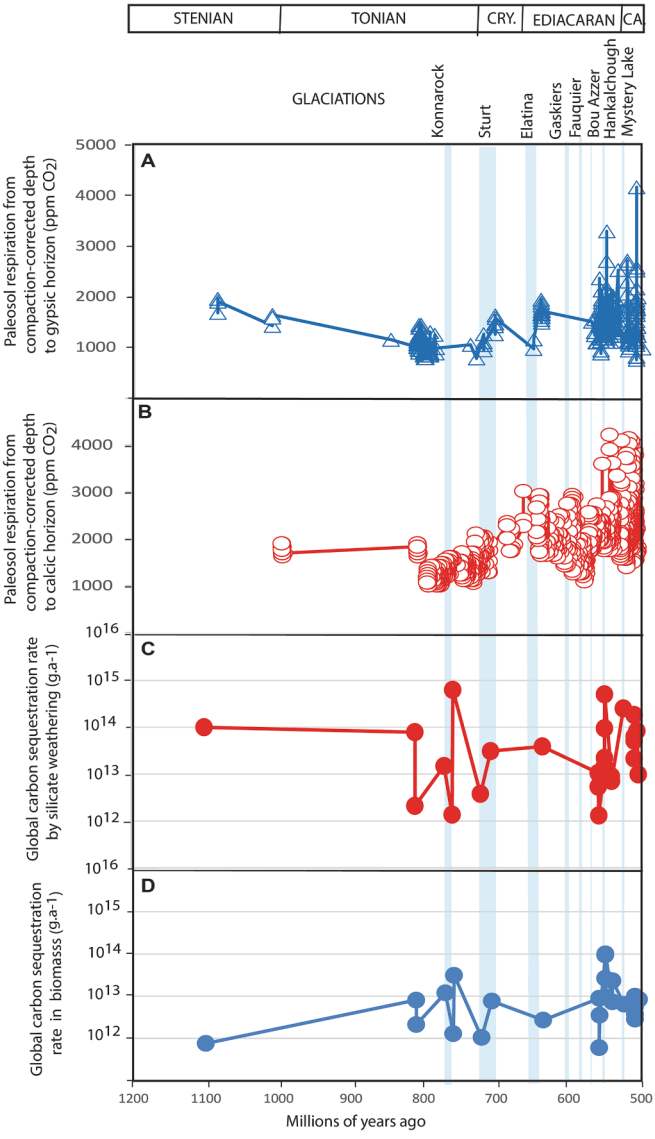

Fig. 7. Mesoproterozoic to Cambrian changes in paleosols: A, paleosol respiration from compaction-corrected depth to gypsic horizons (ppm CO_2); B, paleosol respiration from compaction-corrected depth to calcic horizons (ppm CO_2); C, Global rate of C sequestration by silicate weathering (g.a^{-1}) from loss of Ca + Mg + Na + K normalized for duration and precipitation (mol.mm^{-1}.a^{-1}); D, Global rate of C sequestration in biomass (g.a^{-1}) from loss of P normalized for duration and precipitation (mol.mm^{-1}.a^{-1}).

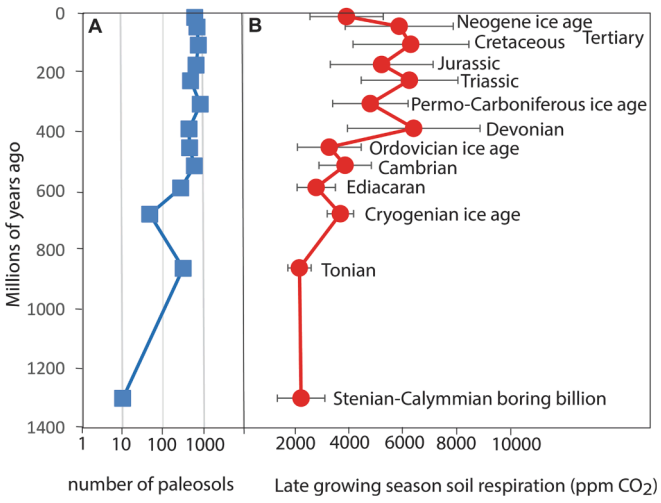

Fig. 8. Late growing season soil respiration increase from Tonian to Cryogenian based on depth to calcic (Bk) horizon of paleosols (A), with numbers of paleosols on which each estimateis based (B). Raw data is in Supplementary Information online.

$$\varepsilon_{i,w} = \left[\frac{\rho_p C_{j,p}}{\rho_w C_{j,w}}\right] - 1 \quad (3)$$

$$\tau_{j,w} = \left[\frac{\rho_w C_{j,w}}{\rho_p C_{j,p}}\right]\left[\varepsilon_{i,w} + 1\right] - 1 \quad (4)$$

Soils and paleosols lose mass with weathering and so have negative strain ($\varepsilon_{i,w} < 0$), and also lose nutrient cations and silica, so have negative mass transfer ($\tau_{j,w} < 0$). Release of soluble alkali and alkaline earth cations and bicarbonate into soil solution by carbonic acid from CO_2 in solution can be simplified to equations 5-8, showing that each mole of alkali and alkaline earth oxides consumed 2 mol of CO_2. Losses of these elements from soils on a molar basis is a proxy for moles of CO_2 consumed by soil over its time of formation (Sheldon, 2006).

$$MgO + 2CO_2 + H_2O \rightarrow Mg^{2+} + 2HCO_3^- \quad (5)$$

$$CaO + 2CO_2 + H_2O \rightarrow Ca^{2+} + 2HCO_3^- \quad (6)$$

$$Na_2O + 2CO_2 + H_2O \rightarrow 2Na^{+} + 2HCO_3^- \quad (7)$$

$$K_2O + 2CO_2 + H_2O \rightarrow 2\,K^{+} + 2HCO_3^- \quad (8)$$

Dissolution of apatite as a source of P can be reduced to equation 5, in which 5 mol of CO_2 generate 3 mol of soluble phosphate effectively lost from the soil (Dorozhkin, 2012). This is a simplification because actual phosphate procurement in soils from relatively insoluble apatite is catalyzed by a variety of carbon-based acid moieties, such as acetic and oxalic acid with higher mole fractions of carbon (Neaman et al., 2005). Again, this is based on mass transfer, including volume loss during soil formation with depth in reconstructed soils as they would have been before burial compaction and metamorphism (Sheldon and Retallack, 2001).

$$Ca_5(PO_4)_3(OH) + 5CO_2 + 15H_2O \rightarrow 5Ca^{2+} + 3PO_4^{3-} + 5HCO_3^- + OH^- + 10H_2O \quad (9)$$

Consumption of CO_2 during soil formation of a compaction corrected paleosol can be calculated using a geochemical model elaborated by Sheldon (2006). Components of these calculations are areas under the curves of depletion of phosphorus in reconstructed paleosol profiles, calculated for the whole profile for a square cm of surface area of the profile, using the following equations.

$$pCO_2 = \frac{F}{A\left[\frac{K_{CO_2}P}{1000} + \kappa\frac{D_{CO_2}\alpha}{L}\right]} \quad (9)$$

$$F = 2\sum \rho_p \frac{C_{j,p}}{100}\int_{Z=0}^{Z=D_{j,w}} \tau_{j,w(z)}\delta Z \quad (10)$$

$$G = 5\sum \rho_p \frac{C_{j,p}}{100}\int_{Z=0}^{Z=D_{j,w}} \tau_{j,w(z)}\delta Z \quad (11)$$

Variables and constants for these calculations besides those needed for equations 9-11 are F (mol CO_2.cm^{-2}) = summed molar mass transfer loss of CaO, MgO, Na_2O and K_2O using equation 9; G (mol CO_2.cm^{-2}) = summed molar mass transfer loss of P using equation 10; Z (cm) = depth in soil represented by analysis corrected for compaction using equation 10; A (years) = duration of soil formation using equations 12 and 13; K_{CO2} (mol./kg.bar) = Henry's Law constant for CO_2 (=0.034, range 0.031–0.0045); P (cm) = mean annual precipitation using equations 14 and 15; κ (s.cm^3.(mol.year)$^{-1}$) = seconds per year divided by volume per mole of gas at standard temperature and pressure (=1,430); D_{CO2} (cm^2.s^{-1}) = diffusion constant for CO_2 in air (=0.162); α (fraction) = ratio of diffusion constant for CO_2 in soil divided by diffusion constant for CO_2 in air (=0.1, range 0.08–0.12); L (cm) = original depth to water table (after decompacted using equation 6).

Degree of weathering increases with duration of soil formation in years (A in kyr), which can be calculated from carbonate nodule diameter (D in cm: r^2 = 0.57, s.e. = 1.8, p=<0.001; Retallack, 2005), or thickness of profile (T in cm: r^2 = 0.79, s.e. = 140, p = 0.01; Retallack, 2022a).

$$A = 3.92D^{0.34} \quad (12)$$

$$A = 4.915S - 343.4 \quad (13)$$

Degree of weathering also increases with mean annual precipitation (P in mm), which can be obtained by the CIA-K proxy (Sheldon et al., 2002), effectively chemical index of alteration without diagenetically problematic K (I as mole fraction: r^2 = 0.72, s.e. = 182, p=<0.0001). Alternatively mean annual precipitation can be estimated from paleosols using compaction-corrected depth to calcic horizon (D in cm: r^2 = 0.52, s.e. = 147, p=<0.0001; Retallack, 2005).

$$P = 221.1e^{0.0197I} \quad (14)$$

$$P = 137.24 + 6.45D - 0.0132^2 \quad (15)$$

Division of molar depletions of equations 10 and 11 by duration of formation, and by mean annual precipitation of the paleosols allows an paleoclimate-normalized rate of nutrient and phosphorus depletion in μmol F.cm^2.mm^{-1}.a^{-1}, where F is the sum of the four alkaline and alkaline earth base, or μmol G.cm^2.mm^{-1}.a^{-1}, where G is the sum of phosphorus depletions. These local paleosol CO_2 consumptions can be extrapolated to global estimates if multiplied by modal mean annual precipitation, which is 758 mm in the modern world (Grieser and Rudolf, 2005). This modal mean annual precipitation may have changed in deep time, but current understanding of paleoprecipitation from calcic and gypsic paleosols shows mainly arid to subhumid estimates (Retallack, 2009a, 2009b) comparable with today (Retallack, 2005; Retallack and Huang, 2010), and the database of Table 1 also includes thick noncalcareous unconformity paleosols of humid climates (Zbinden et al., 1988; Retallack and Mindszenty, 1994; Horodyskyj et al., 2012; Liivamägi et al., 2015). Global sequestration rate (g.a^{-1}) is found by multiplying by 758 the rate of sequestration per mm of precipitation (g mm^{-1} a^{-1}), a fixed factor unlikely to have overwhelmed order of magnitude changes in carbon sequestration needed for global change (Retallack, 2022a, 2022b). Also needed is an estimate of Neoproterozoic land area (Table 1), and these were taken from emergent land of the Neoproterozoic hypsometric curve of Hawkesworth et al. (2017) as a

fraction of the continental area model of Höning and Spohn (2016).

Order of magnitude increases in CO_2 consumption rates (Fig. 7) and soil respiration (Fig. 8) are seen from Tonian to Cryogenian. Rates of depletion normalized for mean annual precipitation and duration of soil formation ($\mu mol.mm^{-1}.a^{-1}$) of up to 0.17 in bioessential phosphorus and 3.4 for total cationic bases (Mg^{2+}, Ca^{2+}, Na^{+}, K^{+}) in Tonian (758 Ma) paleosols (Retallack et al., 2021), are comparable with Ediacaran (550 Ma) paleosols (up to 0.52 for P and 2.6 for total bases; Retallack, 2013b), but greater than earlier Tonian (810 Ma) paleosols (up to 0.04 for P and 0.43 for total bases; Retallack and Mindszenty, 1994). Scaled up to global sequestration (Table 1), there is much variability from paleosol to paleosol (Fig. 7C-D), but this amounts to carbon sequestration of up to 0.1 Pg C (Pg = 10^{15}g) for the Tonian increasing to 0.5 Pg C for the Cryogenian to Cambrian from alkali and alkaline earth cation depletion as a proxy for consumption by silicate weathering, and up to 0.03 Pg for the Tonian increasing to 0.1 Pg for the Cryogenian to Cambrian from P depletion as a proxy for biomass (Retallack, 2022b). These are substantial differences capable of explaining the difference between glaciated and unglaciated Neogene Earth (Retallack, 2022a). They are both short of modern carbon sequestration rates by silicate weathering of 0.3 $PgC.a^{-1}$ and into photosynthetic biomass of 1.7 $PgC.a^{-1}$ (Ciais et al., 2013).

8. Conclusions

This demonstration of increased soil biodiversity and chemical weathering in Arizona (Retallack et al., 2021) and Australia (Retallack, 2021) before the onset of Snowball Earth supports the idea that evolutionary advances in life on land induced this greatest of known glaciations. These newly documented sections can also be used to reconsider alternative explanations for Snowball Earth cooling, such as deep tropical weathering (Hoffman et al., 2017), marine plankton changes (Tzipermann et al., 2011), or voluminous volcanism (Donnadieu et al., 2004; MacDonald and Wordsworth, 2017; Long et al., 2019; Arnscheidt and Rothman, 2020). The upper Chuar Group was deposited at low latitude and at a time of active felsic volcanism (Retallack et al., 2021), supporting those potential causes for increased weathering and carbon consumption on land. Marine facies of the upper Chuar group also show increased biodiversity of microfossils (Porter et al., 2003; Dehler et al., 2005), as would be expected if fertilized from increasingly weathered soils of the source regions.

Tectonic, volcanic, or oceanographic explanations for Snowball onset are not supported by both sections in Australia or Arizona, and there are also other reasons to doubt that these are the only explanations. Pre-Cryogenian continents were not bunched up along the equator but spread through many latitudes (Hoffman et al., 2017). Deep weathering profiles are included in Table 1 and Fig. 7C-D, but also well documented during the earlier Proterozoic and Archean (Rye and Holland, 1998). Voluminous volcanism would have been a source of greenhouse gases rather than a sink (Ciais et al., 2013), so large igneous provinces such as the Franklin Volcanics of Canada (Cox et al., 2016) more likely delayed onset of Snowball Earth than caused it. Basalt flows are sluggishly weathered compared with glacial loess and vitric volcanic ash, as revealed by distinctive landscapes such as the Channeled Scabland of Washington USA (McDonald and Busacca, 1990). Carbon sequestration in soils and ecosystems today is much lower in volcanic arcs and plateaus than in river basins and loess plains (Ciais et al., 2013). Marine upwelling zones supplying nutrients today are limited in area compared with riverine supply, and marine productivity is greatest near shore (Bakun et al., 2015). Thus marine increases in productivity during the Tonian would have depended on terrestrial weathering.

The idea that advances in evolution of life on land induced ice ages is comparable with the view that the Late Ordovician (Hirnantian) ice age was caused by the evolution of non-vascular land plants (Lenton et al., 2012; Retallack, 2015b), that the Permo-Carboniferous ice age was caused by the evolution of trees (Berner, 1997; Retallack, 1997), and that Pleistocene glaciation was caused by coevolution of grasses and grazers (Retallack, 2013a). Snowball Earth may have been much more extensive that these Phanerozoic glaciations because plants and their high productivity ecosystems are more vulnerable to frost than lichens and other fungi envisaged during Snowball Earth. Advancing glaciers have less effect in curtailing productivity and weathering under lichens than plants (Kappen and Schroeter, 1997).

Declaration of Competing Interest

The authors declare that they have no known competing financial interests or personal relationships that could have appeared to influence the work reported in this paper.

Data availability

Data will be made available on request.

Acknowledgments

Ronda Newton facilitated a permit #GRCA-2018-SCI-0048 to work in Grand Canyon National Park, and logistic and debriefing support came from park personnel Rusty Knudson, Mike Impagliazzo, Erick Lundin, Ellen Brennan, Betsy Aurnou, and Jeff Schwartz. Adrian Broz, Larry Lai, and Kevin Gardner helped with field work, and Sophie Cromartie and Renee Gardner with expedition communications. Paul Strother, Eva Stüeken, Karl Karlstrom, Tom Algeo, Wayne Ranney, Susannah Porter, Bonney Bloeser, Bill Schopf, Karl Karlstrom, Laura Crossey, Andy Knoll, and Carol Dehler offered essential information and discussion. Work was funded by a grant from the Sandal Society of the Museum of Natural and Cultural History of the University of Oregon.

Data availability

All data relevant for this work are in this paper and supplementary information.

Appendix A. Supplementary data

Supplementary data to this article can be found online at https://doi.org/10.1016/j.precamres.2022.106952.

References

Agić, H., Cohen, P.A., 2021. Non-pollen palynomorphs in deep time: unravelling the evolution of early eukaryotes. In: McCarthy, F.M.G., Pilkington, P.M., Volik, O., Heyde, A., Cocker, S.L. (eds), Non-pollen palynomorphs in freshwater sediments and their palaeolimnological potential and selected applications. Geol. Soc. London Spec. Publ. 511, 321–342.

Agić, H., Högström, A.E., Moczydłowska, M., Jensen, S., Palacios, T., Meinhold, G., Ebbestad, J.O.R., Taylor, W.L., Høyberget, M., 2019. Organically-preserved multicellular eukaryote from the early Ediacaran Nyborg Formation, Arctic Norway. Sci. Rep. 9(1), 1–12 (2019).

Arnscheidt, C.W., Rothman, D.H., 2020. Routes to global glaciation. Proc. Roy. Soc. London A 476, 20200303.

Bakun, A., Black, B.A., Bograd, S.J., Garcia-Reyes, M., Miller, A.J., Rykaczewski, R.R., Sydeman, W.J., 2015. Anticipated effects of climate change on coastal upwelling ecosystems. Curr. Climate Change Rep. 1, 85–93.

Berner, R.A., 1997. The rise of plants and their effect on weathering and atmospheric CO_2. Science 276, 543–546.

Bobrovskiy, I., Hope, J.M., Ivantsov, A., Nettersheim, B.J., Hallmann, C., Brocks, J.J., 2018. Ancient steroids establish the Ediacaran fossil *Dickinsonia* as one of the earliest animals. Science 361, 1246–1249.

Brady, P.V., Dorn, R.I., Brazel, A.J., Clark, J., Moore, R.B., Glidewell, T., 1999. Direct measurement of the combined effects of lichen, rainfall, and temperature on silicate weathering. Geochim. Cosmochim. Acta 63, 3293–3300.

Breecker, D.O., Retallack, G.J., 2014. Refining the pedogenic carbonate atmospheric CO_2 proxy and application to Miocene CO_2. Palaeogeogr. Palaeoclim. Palaeoec. 406, 1–8.

Brimhall, G.H., Chadwick, O.A., Lewis, C.J., Compston, W., Williams, I.S., Danti, K.J., Dietrich, W.E., Power, M.E., Hendricks, D., Bratt, J., 1992. Deformational mass transport and invasive processes in soil evolution. Science 255, 695–702.

Ciais, P., Sabine, C., Bala, G., Bopp, L., Brovkin, V., Canadell, J., Chhabra, A., DeFries, R., Galloway, J., Heimann, M., Jones, C., Le Quéré, C., Myneni, R.B., Piao, S., Thornton, P., 2013. Carbon and other geochemical cycles. In: Stocker, T.F., Qin, D., Plattner, G.-K., Tignor, M., Allen, S.K., Boschung, J., Nauels, A., Xia, Y., Bex, V., Midgley, P.M. (Eds.), Climate Change 2013: the Physical Science Basis. Cambridge Univ. Press, Cambridge, pp. 465–570.

Cox, G.M., Halverson, G.P., Stevenson, R.K., Vokaty, M., Poirier, A., Kunzmann, M., Li, Z. X., Denyszyn, S.W., Strauss, J.V., Macdonald, F.A., 2016. Continental flood basalt weathering as a trigger for Neoproterozoic Snowball Earth. Earth Planet. Sci. Lett. 446, 89–99.

Dehler, C.M., Elrick, M., Bloch, J.D., Crossey, L.J., Karlstrom, K.E., des Marais, D.D., 2005. High-resolution $\delta^{13}C$ stratigraphy of the Chuar Group (ca. 770–742 Ma), Grand Canyon: Implications for mid-Neoproterozoic climate change. Geol. Soc. Amer. Bull. 117, 32–45.

Donnadieu, Y., Goddćris, Y., Ramstein, G., Nćdćlec, A., Meert, J., 2004. A 'snowball Earth' climate triggered by continental break-up through changes in runoff. Nature 428, 303–306.

Dorozhkin, S.V., 2012. Dissolution mechanism of calcium apatites in acids: A review of literature. World J. Methodology 2, 1–17.

Ewing, S.A., Macalady, J.L., Warren-Rhodes, K., McKay, C.P., Amundson, R., 2008. Changes in the soil C cycle at the arid-hyperarid transition in the Atacama Desert. J. Geophys. Res. Biogeosciences 113, e G02S90.

Gomes, S.I., van Bodegom, P.M., Merckx, V.S., Soudzilovskaia, N.A., 2019. Global distribution patterns of mycoheterotrophy. Global Ecol. Biogeogr. 28, 1133–1145.

Grieser, C.J., Rudolf, B., 2005. A new monthly precipitation climatology for the global land areas for the period 1951 to 2000. German Weather Serv. Offenbach Clim. Status Rep. 2004, 181–190.

Hawkesworth, C.J., Cawood, P.A., Dhuime, B., Kemp, T.I., 2017. Earth's continental lithosphere through time. Ann. Rev. Earth Planet. Sci. 45, 169–198.

Hedges, S.B., 2003. Molecular clocks and a biological trigger for Neoproterozoic Snowball Earth events and the Cambrian explosion. In: Donoghue, P.C.J., Smith, P. M. (Eds.), Telling the Evolutionary Time: Molecular Clocks and the Fossil Record. CRC Press, Boca Raton, pp. 27–40.

Hermann, T.N., Podkovyrov, V.N., 2006. Fungal remains from the Late Riphean. Paleont. J. 40, 207–214.

Hoffman, P.F., Abbot, D.S., Ashkenazy, Y., Benn, D.I., Brocks, J.J., Cohen, P.A., Cox, G. M., Creveling, J.R., Donnadieu, Y., Erwin, D.H., Fairchild, I.J., 2017. Snowball Earth climate dynamics and Cryogenian geology-geobiology. Sci. Adv. 3 (11), e1600983.

Höning, D., Spohn, T., 2016. Continental growth and mantle hydration as intertwined feedback cycles in the thermal evolution of Earth. Phys. Earth Planet. Interiors 255, 27–49.

Horodyskyj, L.B., White, T.S., Kump, L.R., 2012. Substantial biologically mediated phosphorus depletion from the surface of a Middle Cambrian paleosol. Geology 40, 503–506.

Jago, J.B., Gehling, J.G., Paterson, J.R., Brock, G.A., 2012. Comments on Retallack, G.J. 2011: problematic megafossils in Cambrian palaeosols of South Australia. Palaeontology 55, 913–917.

Johnston, D.T., Poulton, S.W., Dehler, C., Porter, S., Husson, J., Canfield, D.E., Knoll, A. H., 2010. An emerging picture of Neoproterozoic ocean chemistry: Insights from the Chuar Group, Grand Canyon, USA. Earth Planet. Sci. Lett. 290, 64–73.

Kappen, L., Schroeter, B., 1997. Activity of lichens under the influence of snow and ice. Proc Nat. Inst. Polar Res. Symp. Polar Biology 1, 163–168.

Kennedy, M., 2013. The nonlinear effects of evolutionary innovation biospheric feedbacks on qualitative environmental change: From the microbial to metazoan world. Amer. Nat. 181, 100–111.

Ku, T.C.W., Kay, J., Browne, E., Martini, A.M., Peters, S.C., Chen, M.D., 2008. Pyritization of iron in tropical coastal sediments: implications for the development of iron, sulfur, and carbon diagenetic properties, Saint Lucia. Lesser Antilles. Marine Geol. 249, 184–205.

Lenton, T.M., Crouch, M., Johnson, M., Pires, N., Dolan, L., 2012. First plants cooled the Ordovician. Nature Geosci. 5, 86–89.

Li, G., Pang, K., Chen, L., Zhou, G., Han, C., Yang, L., Wang, W., Yang, F., Yin, L., 2019. Organic-walled microfossils from the Tonian Tongjiazhuang Formation of the Tumen Group in western Shandong, North China Craton and their biostratigraphic significance. Gondwana Res. 76, 260–289.

Liivamägi, S., Somelar, P., Vircava, I., Mahaney, W.C., Kirs, J., Kirsimäe, K., 2015. Petrology, mineralogy and geochemical climofunctions of the Neoproterozoic Baltic paleosol. Precambrian Res. 256, 170–188.

Liu, Y., Yang, J., Bao, H., Shen, B., Hu, Y., 2020. Large equatorial seasonal cycle during Marinoan snowball Earth. Sci. Adv. 6, eaay2471.

Long, J., Zhang, S., Luo, K., 2019. Cryogenian magmatic activity and early life evolution. Sci. Rep. 9, 6586.

Loron, C.C., François, C., Rainbird, R.H., Turner, E.C., Borensztajn, S., Javaux, E.J., 2019. Early fungi from the Proterozoic era in Arctic Canada. Nature 570, 232–235.

MacDonald, F.A., Wordsworth, R., 2017. Initiation of Snowball Earth with volcanic sulfur aerosol emissions. Geophys. Res. Lett. 44, 1938–1946.

MacLennan, S.A., Eddy, M.P., Merschat, A.J., Mehra, A.K., Crockford, P.W., Maloof, A.C., Southworth, C.S., Schoene, B., 2020. Geologic evidence for an icehouse Earth before the Sturtian global glaciation. Sci. Adv. 6 (24), 6647.

McDonald, E.V., Busacca, A.J., 1990. Interaction between aggrading geomorphic surfaces and the formation of a Late Pleistocene paleosol in the Palouse loess of eastern Washington state. Geomorphology 3, 449–469.

Mitchell, E.A., Charman, D.J., Warner, B.G., 2008. Testate amoebae analysis in ecological and paleoecological studies of wetlands: past, present and future. Biodiversity Conservation 17, 2115–2137.

Neaman, A., Chorover, J., Brantley, S.L., 2005. Implications of the evolution of organic acid moieties for basalt weathering over geologic time. Amer. J. Sci. 305, 147–185.

Porter, S.M., 2016. Tiny vampires in ancient seas: evidence for predation via perforation in fossils from the 780–740 million-year-old Chuar Group, Grand Canyon, USA. Proc. Roy. Soc. B 283, 20160221.

Porter, S.M., Meisterfeld, R., Knoll, A.H., 2003. Vase-shaped microfossils from the Neoproterozoic Chuar Group, Grand Canyon: a classification guided by modern testate amoebae. J. Paleont. 77, 409–429.

Retallack, G.J., 1983. A paleopedological approach to the interpretation of terrestrial sedimentary rocks: the mid-Tertiary fossil soils of Badlands National Park. South Dakota. Bull. Geol. Soc. America 94, 823–840.

Retallack, G.J., 1997. Early forest soils and their role in Devonian global change. Science 276, 583–585.

Retallack, G.J., 2005. Pedogenic carbonate proxies for amount and seasonality of precipitation in paleosols. Geology 33, 333–336.

Retallack, G.J., 2008. Cambrian paleosols and landscapes of South Australia. Australian J. Earth Sci. 55, 1083–1106.

Retallack, G.J., 2009a. Early Paleozoic pedostratigraphy and global events in Australia. Australian J. Earth Sci. 56, 569–584.

Retallack, G.J., 2009b. Greenhouse crises of the past 300 million years. Geol. Soc. Amer. Bull. 121, 1441–1455.

Retallack, G.J., 2011a. Problematic megafossils in Cambrian palaeosols of South Australia. Palaeontology 54, 1223–1242.

Retallack, G.J., 2011b. Neoproterozoic loess and limits to snowball Earth. J. Geol. Soc. London 168, 289–308.

Retallack, G.J., 2012. Reply to comments on Retallack, G.J. 2011: problematic megafossils in Cambrian palaeosols of South Australia. Palaeontology 55, 919–921.

Retallack, G.J., 2013a. Global cooling by grassland soils of the geological past and near future. Ann. Rev. Earth Planet. Sci. 41, 69–86.

Retallack, G.J., 2013b. Ediacaran life on land. Nature 493, 89–92.

Retallack, G.J., 2015a. Acritarch evidence for an Ediacaran adaptive radiation of Fungi. Botanica Pacifica 4, 19–33.

Retallack, G.J., 2015b. Late Ordovician glaciation initiated by early land plant evolution and punctuated by greenhouse mass extinctions. J. Geol. 123, 509–538.

Retallack, G.J., 2019. Ordovician land plants and fungi from Douglas Dam, Tennessee. Palaeobotanist 68, 173–205.

Retallack, G.J., 2020. Boron paleosalinity proxy for deeply buried Paleozoic and Ediacaran fossils. Palaeogeogr. Palaeoclim. Palaeoec. 540, 109536.

Retallack, G.J., 2021. Paleosols and weathering leading up to Snowball Earth in central Australia. Aust. J. Earth Sci. 68, 1122–1148.

Retallack, G.J., 2022a. Soil carbon dioxide planetary thermostat. Astrobiology 22, 116–123.

Retallack, G.J., 2022b. Biotic enhancement of weathering over the past 3.7 billion years. GSA Today 32, 3–6.

Retallack, G.J., Huang, C., 2010. Depth to gypsic horizon as a proxy for paleoprecipitation in paleosols of sedimentary environments. Geology 38, 403–406.

Retallack, G.J., Mindszenty, A., 1994. Well preserved late Precambrian paleosols from northwest Scotland. J. Sedim. Res. 64, 264–281.

Retallack, G.J., Bestland, E.A., Fremd, T.J., 2000. Eocene and Oligocene paleosols and environmental change in central Oregon. Geol. Soc. Amer. Spec. Pap. 344, 192 p.

Retallack, G.J., Wynn, J.G., Fremd, T.J., 2004. Glacial-interglacial-scale paleoclimatic changes without large ice sheets in the Oligocene of central Oregon. Geology 32, 297–300.

Retallack, G.J., Krull, E.S., Thackray, G.D., Parkinson, D., 2013. Problematic urn-shaped fossils from a Paleoproterozoic (2.2 Ga) paleosol in South Africa. Precambrian Res. 235, 71–87.

Retallack, G.J., Gose, B.N., Osterhout, J.T., 2015. Periglacial palaeosols and Cryogenian paleoclimate near Adelaide. South Australia. Precambrian Res. 263, 1–18.

Retallack, G.J., Broz, A.P., Lai, L.S.H., Gardner, K., 2021. Neoproterozoic marine chemostratigraphy, or eustatic sea level change? Palaeogeogr. Palaeoclim. Palaeoec. 562, 110155.

Royer, D.L., 1999. Depth to pedogenic carbonate horizon as a paleoprecipitation indicator? Geology 27, 1123–1126.

Rye, R., Holland, H.D., 1998. Paleosols and the evolution of atmospheric oxygen: a critical review. Amer. J. Sci. 298, 621–672.

Schopf, J.W., Ford, T.D., Breed, W.J., 1973. Microorganisms from the late Precambrian of the Grand Canyon, Arizona. Science 179, 1319–1321.

Schwartzman, D.W., 2017. Life's critical role in the long-term carbon cycle: The biotic enhancement of weathering. AIMS Geosci. 3, 216–238.

Sheldon, N.D., 2006. Precambrian paleosols and atmospheric CO2 levels. Precambr. Res. 147 (1–2), 148–155.

Sheldon, N.D., Retallack, G.J., 2001. Equation for compaction of paleosols due to burial. Geology 29, 247–250.

Sheldon, N.D., Retallack, G.J., Tanaka, S., 2002. Geochemical climofunctions from North American soils and application to paleosols across the Eocene-Oligocene boundary in Oregon. J. Geol. 110, 687–696.

Smith, M.R., 2016. Cord-forming Palaeozoic fungi in terrestrial assemblages. Bot. J. Linnean Soc. 180, 452–460.

Stern, R.J., Miller, N.R., 2018. Did the transition to plate tectonics cause Neoproterozoic Snowball Earth? Terra Nova 30, 87–94.

Strother, P.K., Foster, C., 2021. Fossil record of land plant origins from charophyte algae. Science 373, 792–796.

Strother, P.K., Wellman, C.H., 2016. Palaeoecology of a billion-year-old non-marine cyanobacterium from the Torridon Group and Nonesuch Formation. Palaeontology 59, 89–108.

Strother, P.K., Taylor, W.A., Beck, J.H., Vecoli, M., 2017. Ordovician spore 'thalli'and the evolution of the plant sporophyte. Palynology 41, 57–68.
Taylor, T.N., Krings, M., Taylor, E.L., 2015. Fungal Diversity in the Fossil Record. In: McLaughlin, D.J., Spatafora, J.W. (Eds.), Systematics and Evolution. Springer, Berlin, Heidelberg, pp. 259–278.
Tziperman, E., Halevy, I., Johnston, D.T., Knoll, A.H., Schrag, D.P., 2011. Biologically induced initiation of Neoproterozoic Snowball-Earth events. U.S. Nat. Acad. Sci. 108, 15091–15096.
Van Maldegem, L.M., Sansjofre, P., Weijers, J.W., Wolkenstein, K., Strother, P.K., Wörmer, L., Hefter, J., Nettersheim, B.J., Hoshino, Y., Schouten, S., Damsté, J.S., 2019. Bisnorgammacerane traces predatory pressure and the persistent rise of algal ecosystems after Snowball Earth. Nat. Commun. 10 (1), 1–11.
Woltz, C.R., Porter, S.M., Agić, H., Dehler, C.M., Junium, C.K., Riedman, L.A., Hodgskiss, M.S.W., Wörndle, S., Halverson, G.P., 2021. Total organic carbon and the preservation of organic-walled microfossils in Precambrian shale. Geology 49, 556–560.
Zbinden, E.A., Holland, H.D., Feakes, C.R., Dobos, S.K., 1988. The Sturgeon Falls paleosol and the composition of the atmosphere 1.1 Ga BP. Precambrian Res. 42, 141–163.